Design, Build, and Data Acquisition of Atmospheric Turbulence using Drones

Gihyun Kim

Faculty of Engineering, The University of Hong Kong, Pokfulam Road, Hong Kong, China

Faculty supervisor: Prof. C. H. Liu

Laidlaw Undergraduate Research and Leadership Programme, August 2026

Drones are often devised as a possible solution to measuring wind at lower altitudes as they are mostly small, portable, and able to maintain a specific flight altitude. The main issue is that the flow induced by the propellers that allow drones to achieve fixed-altitude flight push past the very sensor meant to measure the wind; while an established fix is to move the sensor well clear of that flow, doing so increases the total size and mass of the airframe. Hence, the proposed system involves a wind-measuring system built around a small consumer drone, mounting an ultrasonic anemometer above the airframe on a short carbon-fiber rod, which returns stable 40 Hz recordings at various height levels capturing atmospheric data for further analysis.

Keywords: unmanned aerial vehicle; ultrasonic anemometry; rotor-induced flow; wind profiling

1. Introduction

The atmospheric boundary layer is defined as the part of the atmosphere that interacts with the ground, and the momentum, heat, and pollutants exchanged across it are carried mostly by turbulence rather than by the smooth average flow.[1] Therefore, characterization of the boundary layer requires measurements of both the average wind at various heights and the rapid fluctuations about the mean. For most of the past century, these have been obtained through meteorological towers, which provide continuous high-frequency data from a known fixed altitude, and are thus the basis of the classical near-surface turbulence description.[2] The major limitation is structural: a mast samples data at a fixed height and location, is immobile after deployment, and costs enough to rarely form a network. There are alternative solutions that come with their own sets of limitations. For instance, radiosondes extend the measurements to higher altitudes but give a single profile that drifts away and is not recovered, while lidar and sodar are able to measure continuously without a mast but average each value over a sample volume, which smooths out the sharp changes that make the lowest hundred meters dynamically significant. There is thus a gap between the highest feasible mast and the less useful radio sounding, which is poorly covered by current instruments.

Small Unmanned Aerial Vehicles (UAVs) offer a way to fill this gap, providing an ability to both hover at specific altitudes and to adjust their position, and the methods available for measuring wind from them have been reviewed in detail.[3] Intercomparison campaigns that fly many systems against a common reference tower report both meaningful measurements and differences between systems that trace to the platform itself and to how the sensor is configured and integrated into it, with sonic anemometers on multirotor aircraft giving the most accurate winds.[4,5] From this, two main approaches have been developed. The first is indirect, in which the aircraft infers the direction and strength of the wind from its own tilt, as a stationary drone must be leaned into the wind. The calibrated fleet gives good agreement with tower anemometers, with this technique being developed further to obtain all three wind components (u, v, w) using only the flight-control data.[6,7] The key weakness is that wind-tunnel testing shows the error growing several-fold between steady and rapidly changing flow,[8] which is especially important when the measurement target is the turbulence itself. The second is direct, which involves carrying an anemometer on board. This approach gives true high-frequency data independent of the aerodynamic model, but runs into the aircraft's own downwash, since a sensor installed near the aircraft body measures the disturbed, propeller-induced flow (PIF). Flow visualization water-tunnel tests of a quadcopter, simulations validated against lidar, and numerical analysis of several airframes agree that the sensor should be placed sufficiently far from the flow of the rotors, with the specific distance depending on the aircraft and the rotor's size and design.[9–11]

The field has responded by designing larger aircraft, with the sonic anemometer slung below the drone or installed on a mast and pole placed several tens of centimeters away from the rotor flow on airframes thus weighing from five to nearly thirty kilograms.[12–14] Such configurations work well, but are heavy, costly, and are subject to stricter flight regulations, meaning loss of most of the benefits of drone platforms. Even with lighter aircrafts, there are tradeoffs with a sub-kilogram drone with a thermal anemometer mounted right above its body showing persistent downward flow, thus requiring a correction for proper use[15]; other devised solutions involve removing the anemometer entirely.[16] However, the applications that would benefit the most from the light platform, such as the mapping of the flow in the urban canyons, wind field measurements around the turbines, and the survey of a site prior to tower installation, require measurements at many different points.[17–19] Instead of increasing the size of the aircraft in order to accommodate the correctly placed sensor, this study proposes keeping the consumer airframe and accepts the resulting limitations. Here we present a drone-mounted sonic anemometer mounted on a 915 g quadcopter, tested in still air at ten different distances from the rotor flow, including a repeatability test whether the difference between the lengths exceeds day-to-day variation, performed in stepped altitude profiles up to 120 meters, and described with conclusions supported by experiments.

2. Results

2.1. Drone-mounted sonic anemometer design

The structure of the drone-mounted ultrasonic anemometer is illustrated in **Figure 1a**, with the assembled system used for flight tests shown in **Figure 1b**. A LI-550 TriSonica Mini ultrasonic anemometer is held at the top of a vertical carbon-fiber rod attached to a 3D-printed tray, designed using SolidWorks, on the upper side of a DJI Mavic 3E drone alongside a custom-printed circuit board (PCB), which logs the flight test data from the anemometer into a dedicated storage unit. The battery sits on top of a 3D-printed casing and is hung at the bottom of the drone, allowing the instrument to log continuously without drawing power from the aircraft and the recording to survive independently of the flight controller's status. All 3D-printed parts were made using PETG and later strapped together. The carbon-fiber rod is 17.5cm long, making the total length from the center of the anemometer to the propellers 30cm – the optimization of this chosen length is further discussed in Section 3.1. The total weight of the airframe, as shown in **Table 1,** is 1.243kg with the total sensor package weighing 328.3g. Each component's weight was minimized to better the endurance and stability during each flight and although the final weight is above the maximum stated takeoff weight of the manufacturer, it was shown to be able to fly stably and collect data at each height.[20]

Component	**Mass (g)**
Anemometer (LI-550 TriSonica Mini, nominal)	55.0
3D-printed parts (PETG)	40.9
Signal-conditioning board	39.1
Carbon-fiber rod (17.5 cm)	7.4
Miscellaneous (wiring, fasteners, adhesive)	35.9
Package excluding battery	178.3
Battery	150.0
Sensor package total	**328.3**
DJI Mavic 3E airframe	915.0
Total mass	**1,243.3**

Table 1. Mass breakdown of the sensor package. Components were weighed individually on a laboratory balance and are reported to 0.1 g. The anemometer entry is its nominal mass. Miscellaneous covers wiring, fasteners, connectors and adhesive.

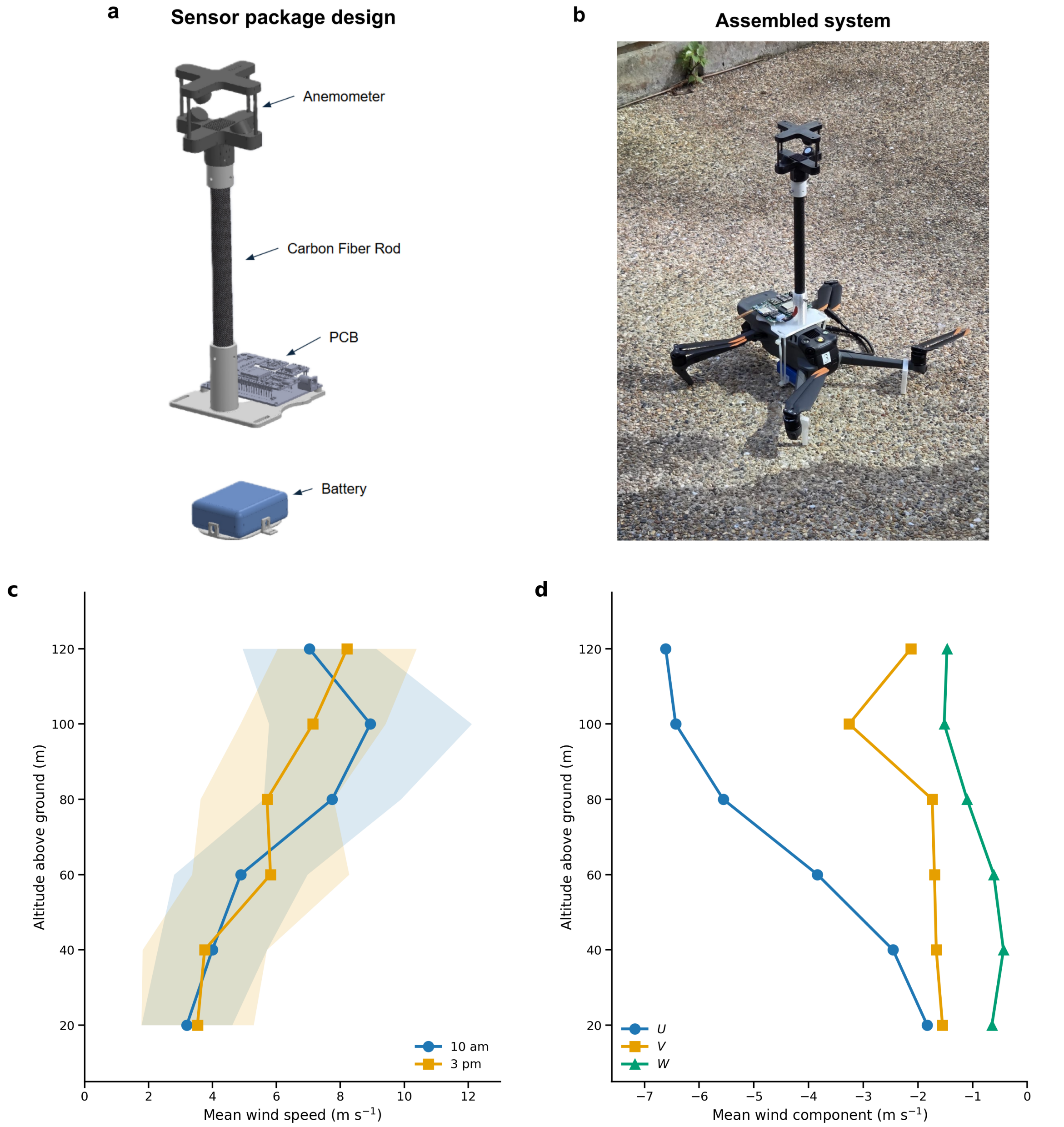

Figure 1. The drone-mounted sonic anemometer and the records it returned. **a**, The sensor package: anemometer, carbon-fiber rod, custom PCB, and battery. **b**, The assembled system on the DJI Mavic 3E. **c**, Mean three-dimensional speed magnitude at each nominal hover height for the morning and afternoon flights; shaded bands are one standard deviation of the readings within that hover. **d**, Mean velocity components across the two sessions against height, in the sensor's own frame of reference and averaged across the two flights.

2.2. Measurement principle

The anemometer determines ultrasonic pulses travelling in opposite directions between three pairs of opposite transducers, and the difference in their respective travel times gives the wind velocity vector component along this path. Thus, the data of the three velocity components are collected at up to 40 Hz without any moving parts or aerodynamic model. Since the length of the vector is independent of its direction, what is measured is the three-dimensional speed magnitude, not the components thereof, whose interpretation would necessitate verification of the mounting transformation. For the outdoor flight sessions, the wind profiles at heights 40, 60, 80, 100 and 120 meters above ground, followed by 20 meters, were measured in that order with the drone holding steady flight for approximately 5 minutes at each altitude. This procedure was carried out twice on the same day at 10:00 and 15:00 Hong Kong Time. Steady altitude holds were detected automatically from the barometric pressure record logged by the anemometer.

3. Analysis

3.1. Rotor-induced flow and rod length selection

The effect of rod length on the reported anemometer data was measured through comparing the baseline wind speed (i.e. the wind speed in the enclosed area without the propellers on) and the wind speed the instrument records during the flight. The drone was placed to hover at approximately 3 m inside a large closed space, where the true wind is close to zero; hence, any variation from the baseline was deemed to be the PIF measured by the anemometer. A continuous record was collected for each of the ten rods with lengths varying from 5 cm to 30 cm. Then, all measurements for a particular rod were processed by computing the mean reading and its variance into a single root-mean-square (RMS) value, see **Table 2 and figure 2a**.

$$S_{RMS} = \sqrt{\bar{S}^2 + \sigma^2} = \sqrt{\frac{1}{n}\sum_{i=1}^{n} S_i^2} \qquad (1)$$

Here S_i are the n samples of indicated speed, $\bar{S}$ their mean and σ their standard deviation.

The choice of RMS as the summary statistic is dictated by the conditions of the measurement. With the wind still, the true wind velocity is zero, and therefore each reading is essentially an error from the true value, with the configuration capable of behaving either by maintaining a stable error at some nonzero offset or by oscillating at zero offset with the samples oscillating: the mean will not detect the second type of malfunction and the standard deviation will not detect the first type. The square root of the sum of squares of the two provides for the root mean square of the actual samples so that the offset is treated identically to the oscillation, provided that the offset is relative to zero. With the wind blowing, the formula will no longer describe an error of the true value; hence, the outdoors hovering configurations in Section 3.2 are reported separately.

The indoor test results, shown in Table 2, show that the propellers-on values are relatively high, ranging roughly from 0.5 to 0.9 $\mathrm{m\,s^{-1}}$. With the propellers stopped, the identical measurement gives 0.0765

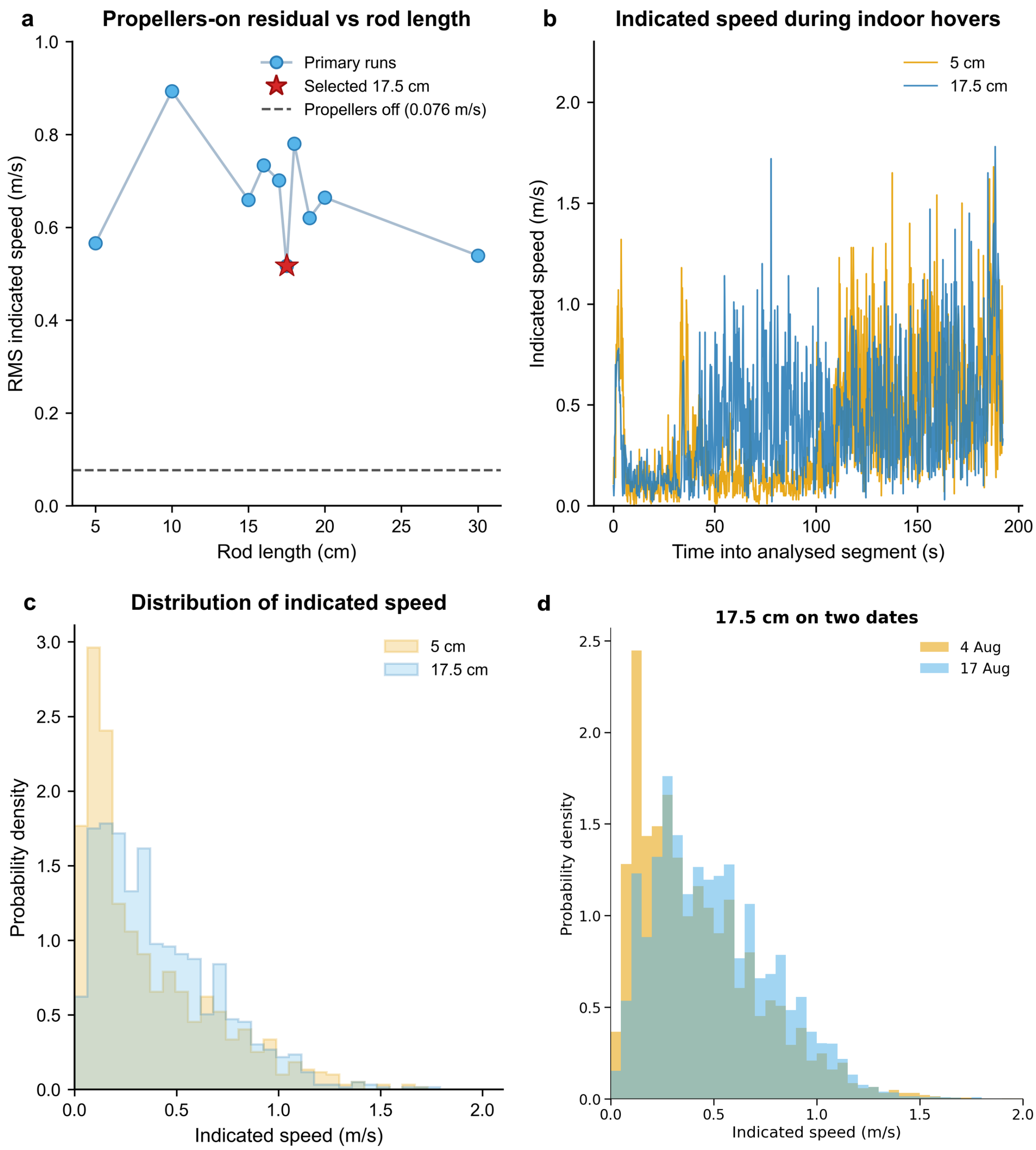

Figure 2. Indoor characterization of rotor-induced flow against rod length. a, RMS indicated speed for the ten propellers-on runs; the star marks the 17.5 cm configuration used outdoors and the dashed line the measured propellers-off background. **b**, Indicated speed over time for the 5 cm and 17.5 cm runs. **c**, The same two runs as distributions. **d**, The 17.5 cm configuration recorded on 4 August and repeated on 17 August, as distributions.

m s^{-1} shown by the dashed line in **Figure 2a**. Any number that exceeds this during flight is deemed to be generated by the operation of the aircraft. The minimum for the flight test case was 0.516 m s^{-1} from the rod distance of 17.5 cm; a repeatability test showed a slight increase of RMS to 0.580 m s^{-1} but the difference standard deviation, interquartile range, and 99th percentile were with all values lying within 0.008, 0.01, 0.06 m s^{-1}, respectively.

Rod length	**Samples / duration (s)**	**Mean (m s^{-1})**	**Standard deviation (m s^{-1})**	**RMS indicated speed (m s^{-1})**
5.0 cm	8,714 / 217.8	0.414	0.385	0.565
10.0 cm	5,486 / 137.2	0.762	0.477	0.899
15.0 cm	5,166 / 129.2	0.564	0.342	0.660
16.0 cm	6,356 / 158.9	0.638	0.370	0.737
17.0 cm	5,499 / 137.5	0.604	0.361	0.704
17.5 cm	**7,597 / 189.9**	**0.421**	**0.298**	**0.516**
18.0 cm	5,731 / 143.3	0.688	0.376	0.784
19.0 cm	5,323 / 133.1	0.534	0.319	0.622
20.0 cm	5,674 / 141.8	0.586	0.321	0.668
30.0 cm	324 / 8.1	0.488	0.253	0.550
Propellers off	5,704 / 142.6	0.066	0.038	0.0765

Table 2. Indoor rod-length runs and the propellers-off background. Each row is one continuous hover at approximately 3 m. RMS indicated speed is $\sqrt{\text{mean}^2+\text{s.d.}^2}$ over the propellers-on segment of the run.

The final selection of rod length was mainly determined by a combination of test results and mechanical restrictions. Rod lengths over 20 cm caused the aircraft to be unstable during flight with near-ground flights possible, but altitudes of over 5 m, the structure oscillated violently, rendering recording any accurate data impossible, which is why the 30 cm row in Table 2 represents only 8.1s of data against the two to four minutes for all other configurations. Therefore, out of the various lengths tested, the rod length of 17.5 cm, and a total distance of 30 cm from the center of the anemometer to the propellers, was deemed to minimally influence the anemometer readings and was selected as the optimal rod length to conduct future flight sessions.

To further illustrate the choice of the 17.5 cm rod, **Figures 2b and 2c** show the two configurations with the smallest residuals among those having complete records: 5 cm and 17.5 cm. Their mean indicated speeds are closely comparable, being 0.414 and 0.421 m s^{-1} correspondingly; the amplitudes of fluctuation, however, are different at 0.385 and 0.298 m s^{-1}. Thus, the two configurations function at approximately the same level, but the 5 cm rod exhibits much greater variability and unstableness in data measurement, allowing for increased consistency in subsequent data analysis.

The variation of the 17.5cm rod was also shown to be closely reproducible with two different tests at different dates of 4th August and repeated on 17 August under same conditions yielded similar results with the standard deviation, interquartile range (IQR), and the 99th percentile all agreeing to within 0.008, 0.01, and 0.06 m s^{-1} (**Figure 2d**). The central tendency varies slightly more from 0.516 to 0.580 m s^{-1} but was within the comparable range of other rod lengths.

3.2. Wind profiles in the lower boundary layer

The sequences described in Section 2.2 were flown twice on the same day with the rod fixed at 17.5 cm. The comparisons of the morning versus the afternoon wind mean speeds are shown in **Figure 1c** with the shaded bands representing the dispersion of the readings within each hover.

Neither profile is shown to increase monotonically with height with the morning record decreasing between 100 and 120 m, and the afternoon record showing a slight decrease from 60 to 80 m. The largest discrepancies between the two sequences occur at 80 and 100 m, where the flights differ by 2.04 and 1.80 $\mathrm{m\,s^{-1}}$ respectively.

In **Figure 1d**, the mean components of u, v, and w in the sensor frame as a function of height are shown; all three channels are shown to be negative throughout the profile. The streamwise channel explains the height dependency, with its increase from $-1.83\ \mathrm{m\,s^{-1}}$ at 20 m to $-6.61\ \mathrm{m\,s^{-1}}$ at 120 m, while the other two channels vary from -0.4 to $-3.3\ \mathrm{m\,s^{-1}}$ within the same height range.

3.3. Turbulence statistics and data analysis

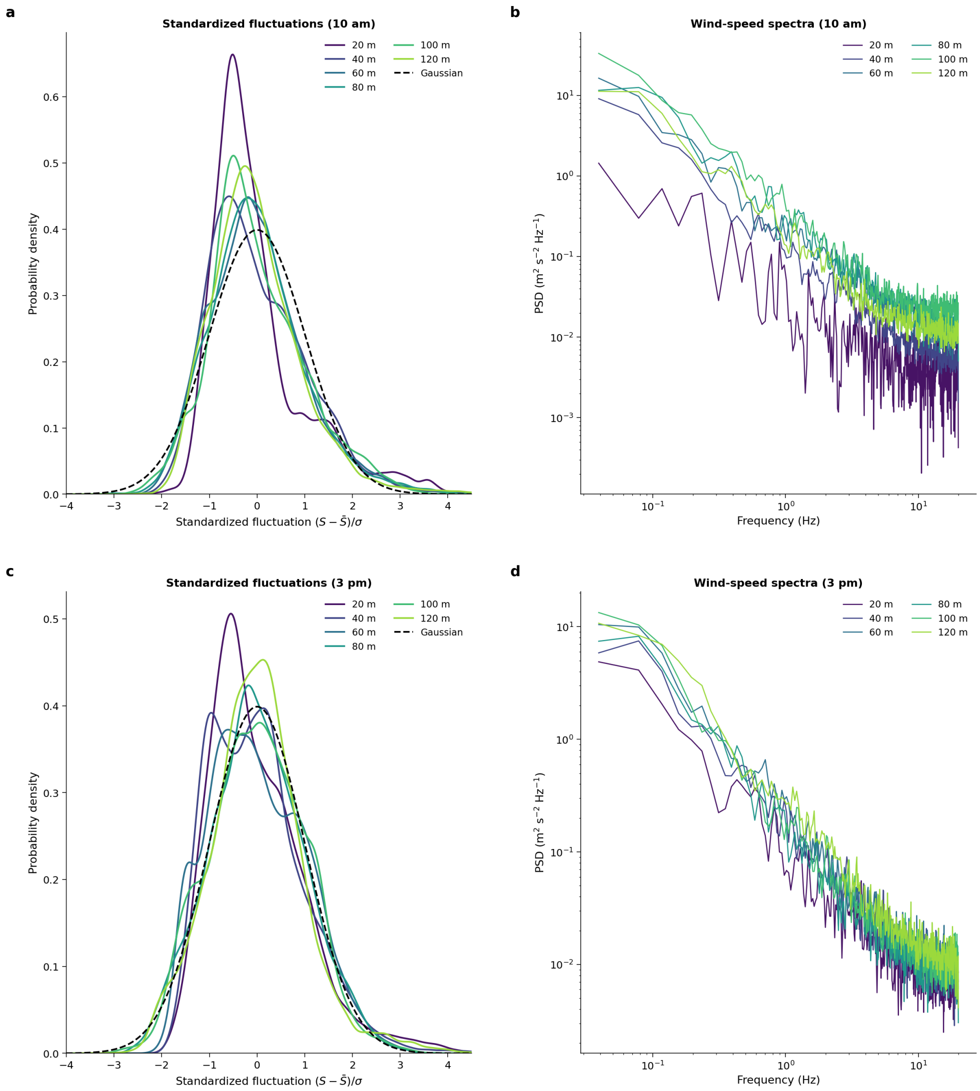

Figure 3. Fluctuation statistics from both outdoor flights. **a**, Distributions of standardised wind-speed fluctuations for the morning holds, with a unit Gaussian for comparison. **b**, Welch power spectra for the same morning holds. **c**, **d**, The corresponding distributions and spectra for the afternoon holds.

The fluctuations found in each hover provide information which is not revealed by the mean value, and **Figures 3a** and **3c** show those fluctuations for both outdoor test flights. Each hover is centred on its own mean and scaled by its own standard deviation, such that the six altitudes may be overlaid, and its asymmetry and tail weight are measured by the skewness g_1 and the Pearson kurtosis β_2, which take the values 0 and 3, respectively, for a Gaussian distribution.

$$z_i = \frac{S_i - \bar{S}}{\sigma} \tag{2}$$

$$g_1 = \frac{1}{n\sigma^3}\sum_{i=1}^{n}\left(S_i - \bar{S}\right)^3, \qquad \beta_2 = \frac{1}{n\sigma^4}\sum_{i=1}^{n}\left(S_i - \bar{S}\right)^4 \tag{3}$$

In the morning, the distributions are positively skewed, with skewness values lying between 0.564 and 1.461, and all carry tails heavier than Gaussian, with kurtosis between 3.34 and 7.28 compared to the value of 3 for a Gaussian distribution. The afternoon distributions show weaker skewness and kurtosis with skewness falling to 0.07 at 100 m and kurtosis to 2.55 at 60 m, such that three of the six afternoon hovers are light tailed compared to Gaussian and two heights, 80m and 100m show near zero skewness. Therefore, intermittent gusts appear to be characteristic of the morning record but not of the platform or the site itself.

Theoretical predictions for turbulence imply that the fluctuation energy decays with frequency following a $-5/3$ power law over an intermediate range of scales.[2]

$$E(f) \propto f^{-5/3} \tag{4}$$

To estimate spectra by Welch's method, we apply least squares to logarithmic axis plots, which makes the fitted relationship a straight line, with a slope of $-5/3$ as shown in equation (4). Least-squares fits for data between 0.2 to 2.5 Hz yielded a slope range of -1.17 to -1.58 in the morning and between -1.21 and -1.51 in the afternoon, all shallower than that value. For goodness of fit measures, afternoon results ranged from 0.83 to 0.93, while morning values were highly variable, ranging from 0.49 at 20 m to 0.95 at 100 m. Both records therefore decay in a manner consistent with developed turbulence (**Figures 3b** and **3d**).

Several limitations affect our results in the study. First the indoor value may not be a truly accurate figure, since the absence of a reference anemometer causes aggregation of PIF, ambient air flow, vibration, aircraft motion, and sensor noise, all into a single measurement. Second, the ranking of rod lengths may lack resolution as out of nine possible intervals, eight are below the 0.064 $\mathrm{m\,s^{-1}}$ difference for the 17.5cm measurement in different test sessions. Third, outdoors, each flight configuration was performed once in the same altitude order, making it impossible to distinguish the effect of temporal evolution from the height dependency, thus precluding derivation of the profile shape or confirmation of differences between flights as a diurnal signal. Lastly, only the sensor frame components of **Figure 1d** were captured, while compass direction is difficult to verify. Addressing these limitations would necessitate another test campaign alongside a calibrated reference anemometer at designated heights.

4. Conclusion

For this research, we investigated the performance of a system composed of an ultrasonic anemometer attached to a commercial quadcopter drone system. We performed test flights both indoors and outdoors at elevations up to 120 meters above ground level. Analysis has shown that there exists an interference flux created by the propellers of the unmanned aerial vehicle that causes measurements to deviate significantly from the idle state. The smallest interference flux was noted in the 17.5 centimeter model, whose dispersion properties were also reproduced accurately within 0.06 m/s during repeatability tests. Wind velocities increased at greater elevations, exhibiting positive skewness and thick tails in the morning hours, transitioning into a Gaussian-like distribution in the afternoon.

5. Experimental Methods

Indoor sessions were conducted on 4, 5, 14 and 17th August. The drone hovered at a height of around 3 meters inside a large, enclosed space, and only data from when the drone reached its target altitude were considered. Similarly, for the outdoor recordings, we discarded any climb segments between the different test heights and kept only the segments when the drone was at its intended altitude. Outdoor speeds were calculated according to the measurements without subtracting the indoor residual speed as one cannot take away a scalar figure from a vector. To find spectral densities, we employed Welch's approach, and we determined the value of the exponent in equation (4) via a least squares fit on logarithmic axis. We recorded data at around 40 Hz, and our sensor's manufacturer specifies an accuracy of ± 0.2 m/s under 10 m/s; however, note that this value applies strictly to the bare sensor, not to the setup.[21]

Acknowledgements

This work was carried out under the Laidlaw Undergraduate Research and Leadership Scholarship at the University of Hong Kong. Special thanks to Prof. C. H. Liu for supervision and the Faculty of Engineering for support.

References

1. Stull, R. B. *An Introduction to Boundary Layer Meteorology*. Springer Netherlands, Dordrecht (1988). doi:10.1007/978-94-009-3027-8

2. Kaimal, J. C., Wyngaard, J. C., Izumi, Y. & Coté, O. R. Spectral characteristics of surface-layer turbulence. *Quarterly Journal of the Royal Meteorological Society* 98, 563–589 (1972). doi:10.1002/qj.49709841707

3. Soltaninezhad, M., Monsorno, R. & Tondini, S. A review of methods and challenges for wind measurement by small unmanned aerial vehicles. *Meteorological Applications* 32, e70065 (2025). doi:10.1002/met.70065

4. Barbieri, L. et al. Intercomparison of small unmanned aircraft system (sUAS) measurements for atmospheric science during the LAPSE-RATE campaign. *Sensors* 19, 2179 (2019). doi:10.3390/s19092179

5. de Boer, G. et al. Evaluation and intercomparison of small uncrewed aircraft systems used for atmospheric research. *Journal of Atmospheric and Oceanic Technology* 41, 127–145 (2024). doi:10.1175/JTECH-D-23-0067.1

6. Wetz, T., Wildmann, N. & Beyrich, F. Distributed wind measurements with multiple quadrotor unmanned aerial vehicles in the atmospheric boundary layer. *Atmospheric Measurement Techniques* 14, 3795–3814 (2021). doi:10.5194/amt-14-3795-2021

7. Wildmann, N. & Wetz, T. Towards vertical wind and turbulent flux estimation with multicopter uncrewed aircraft systems. *Atmospheric Measurement Techniques* 15, 5465–5477 (2022). doi:10.5194/amt-15-5465-2022

8. Kistner, J., Neuhaus, L. & Wildmann, N. High-resolution wind speed measurements with quadcopter uncrewed aerial systems: calibration and verification in a wind tunnel with an active grid. *Atmospheric Measurement Techniques* 17, 4941–4955 (2024). doi:10.5194/amt-17-4941-2024

9. Wilson, T. C., Brenner, J., Morrison, Z., Jacob, J. D. & Elbing, B. R. Wind speed statistics from a small UAS and its sensitivity to sensor location. *Atmosphere* 13, 443 (2022). doi:10.3390/atmos13030443

10. Jin, L., Ghirardelli, M., Mann, J., Sjöholm, M., Kral, S. T. & Reuder, J. Rotary-wing drone-induced flow: comparison of simulations with lidar measurements. *Atmospheric Measurement Techniques* 17, 2721–2737 (2024). doi:10.5194/amt-17-2721-2024

11. Page, G. C. & Bailey, S. C. C. Numerical investigation of the wind field disturbance around small rotorcraft uncrewed aerial vehicles. *Drones* 9, 857 (2025). doi:10.3390/drones9120857

12. Ghirardelli, M., Kral, S. T., Cheynet, E. & Reuder, J. SAMURAI-S: sonic anemometer on a multi-rotor drone for atmospheric turbulence investigation in a sling load configuration. *Atmospheric Measurement Techniques* 18, 2103–2124 (2025). doi:10.5194/amt-18-2103-2025

13. Yang, Y. et al. A correction algorithm for rotor-induced airflow and flight attitude changes during three-dimensional wind speed measurements made from a rotary unoccupied aerial vehicle. *Atmospheric Measurement Techniques* 18, 3035–3050 (2025). doi:10.5194/amt-18-3035-2025

14. Sriyasawin, K., Sumpavakup, C. & Sridech, W. Design and development of multirotor mounted with 3D ultrasonic anemometer for wind assessment. *Applied Mechanics and Materials* 923, 11–17 (2024). doi:10.4028/p-vf7qud

15. Inoue, J. & Sato, K. Wind speed measurement by an inexpensive and lightweight thermal anemometer on a small UAV. *Drones* 6, 289 (2022). doi:10.3390/drones6100289

16. Segales, A. R., Greene, B. R., Bell, T. M., Doyle, W., Martin, J. J., Pillar-Little, E. A. & Chilson, P. B. The CopterSonde: an insight into the development of a smart unmanned aircraft system for atmospheric boundary layer research. *Atmospheric Measurement Techniques* 13, 2833–2848 (2020). doi:10.5194/amt-13-2833-2020

17. Sekula, P., Zimnoch, M., Bartyzel, J., Bokwa, A., Kud, M. & Necki, J. Ultra-light airborne measurement system for investigation of urban boundary layer dynamics. *Sensors* 21, 2920 (2021). doi:10.3390/s21092920

18. Pu, O., Yuan, B., Li, Z., Bao, T., Chen, Z., Yang, L., Qin, H. & Li, Z. Research on the characteristics of urban building cluster wind field based on UAV wind measurement. *Buildings* 13, 3109 (2023). doi:10.3390/buildings13123109

19. Wetz, T. & Wildmann, N. Multi-point in situ measurements of turbulent flow in a wind turbine wake and inflow with a fleet of uncrewed aerial systems. *Wind Energy Science* 8, 515–534 (2023). doi:10.5194/wes-8-515-2023

20. DJI. *Mavic 3 Enterprise Series: Specifications*. DJI, Shenzhen (accessed 29 August 2026).

21. LI-COR Environmental. *LI-550 TriSonica Mini Wind and Weather Sensor: Specifications*. LI-COR Environmental, Lincoln, Nebraska (accessed 29 August 2026).